Spin pumping in strongly coupled magnon-photon systems

H. Maier-Flaig,[1,2,*] M. Harder,[3] R. Gross,[1,2,4] H. Huebl,[1,2,4] and S. T. B. Goennenwein[1,2,4,†]

[1]*Walther-Meißner-Institut, Bayerische Akademie der Wissenschaften, 85748 Garching, Germany*

[2]*Physik-Department, Technische Universität München, 85748 Garching, Germany*

[3]*Department of Physics and Astronomy, University of Manitoba, Winnipeg, Canada R3T 2N2*

[4]*Nanosystems Initiative Munich, Schellingstraße 4, 80799 München, Germany*

(Received 22 January 2016; revised manuscript received 2 August 2016; published 30 August 2016)

We experimentally investigate magnon polaritons arising in ferrimagnetic resonance experiments in a microwave cavity with a tunable quality factor. To this end, we simultaneously measure the electrically detected spin pumping signal and the microwave reflection (the ferrimagnetic resonance signal) of a yttrium iron garnet (YIG)/platinum (Pt) bilayer in the microwave cavity. The coupling strength of the fundamental magnetic resonance mode and the cavity is determined from the microwave reflection data. All features of the magnetic resonance spectra predicted by first principle calculations and an input-output formalism agree with our experimental observations. By changing the decay rate of the cavity at constant magnon-photon coupling rate, we experimentally tune in and out of the strong coupling regime and successfully model the corresponding change of the spin pumping signal and microwave reflection. Furthermore, we observe the coupling and spin pumping of several spin wave modes and provide a quantitative analysis of their coupling rates to the cavity.

DOI: 10.1103/PhysRevB.94.054433

I. INTRODUCTION

Motivated by the vision of hybrid quantum information systems combining the fast manipulation rates of superconducting qubits and the long coherence times of spin ensembles, strong spin-photon coupling is a major goal of quantum information memory applications. Coherent information exchange between microwave cavity photons and a spin ensemble was initially demonstrated for paramagnetic systems [1–3], but only recently has this concept been transferred to magnetically ordered systems, where coupling rates of hundreds of megahertz can be achieved [4–8]. Utilizing the flexibility of exchange coupled magnetically ordered systems, more complex architectures involving multiple magnetic elements have already been developed [9,10]. Additionally, magnetically ordered systems allow to study classical strong coupling physics even at room temperatures [5,6,8–11].

Moreover, a key advantage of magnetically ordered systems over their paramagnetic counterparts—which has yet to be fully explored—is the ability to probe magnetic excitations electrically through spin pumping and the inverse spin Hall effect. Spin pumping, in general, relies on ferromagnet/normal metal (FM/NM) heterostructures and has been demonstrated for a wide variety of material combinations [12]. Under resonant absorption of microwaves, the precessing magnetization in the ferromagnet sources a spin current into the normal metal, where it is converted into a charge current via the inverse spin Hall effect. This spin Hall charge current is then detected. In ferromagnetic insulator (FMI)-based FMI/NM heterostructures, charge current signals from the rectification of the microwave electric field are very small [13], leading to a dominant spin pumping/spin Hall signal. This has led to much research on FMI/NM heterostructures, of which the yttrium iron garnet (YIG)/platinum (Pt) bilayers we use are a prime example. Spin pumping is a well understood effect for weak photon-magnon coupling [12,14], i.e., for situations where the decay rates of the cavity and the magnetic system are larger than the photon-magnon coupling strength. However, the large spin density of YIG and the resulting large effective coupling strength allows one to reach the strong coupling regime also in typical spin pumping experiments. The experimental observation [15] and theoretical treatment [16,17] of spin pumping in a strongly coupled magnon-photon system has only recently been performed. These results suggest that combining spin pumping and strong magnon-photon coupling may enable the control and electrical readout of quantum states in ferromagnets using a hybrid architecture. Experiments directly linking spin pumping in the weak and strong coupling regime are, however, still missing. Such experiments are one important step towards understanding the functional principle and key requirements for such a hybrid architecture.

In this paper, we present a systematic study of the interplay of magnons and photons in a magnetic resonance experiment in a YIG/Pt bilayer mounted in a commercial electron paramagnetic resonance cavity. We measure both the microwave reflection spectra and the electrically detected spin pumping signal in the system. The tunable cavity quality factor allows us to systematically move in and out of the strong coupling regime. Measurements with high magnetic field and frequency resolution allow us to clearly observe the coupling of spin wave modes with the hybridized mode formed by the cavity and the fundamental ferromagnetic resonance mode, i.e., the Kittel mode. We explore a different approach as recently used by Zhang *et al.* [8]: In our setup, instead of tuning the cavity frequency we tune its decay rate while the effective magnon-photon coupling rate and the magnon decay rate stay constant. We thus achieve a transition from the strong coupling regime where the decay rates of spin and cavity system are both considerably smaller than the effective coupling rate, to the weak coupling regime where the cavity decay rate is much higher than the magnon-photon coupling

*hannes.maier-flaig@wmi.badw.de

†Current address: Institut für Festkörperphysik, Technische Universität Dresden, 01062 Dresden, Germany.

rate. This regime is also called the regime of magnetically induced transparency (MIT) [8].

This paper is organized as follows: In Sec. II we review the general theory of the coupled magnon-photon system and the main features of spin pumping in the case of strong coupling. In Sec. III we describe the experimental details of recording the microwave reflection of the system as a function of frequency and applied magnetic field while simultaneously recording the DC spin pumping voltage across the Pt. Finally in Sec. IV we present our observation of strong coupling between the cavity mode and both the fundamental magnetic resonance and standing spin wave modes. We also demonstrate the transition from strong to weak coupling by tuning the cavity linewidth and discuss the difference in the experimental spin pumping signature in both the strong and weak regimes.

II. THEORY

A. Photon-magnon dispersion

Conventionally, ferromagnetic resonance (FMR) is modeled in terms of the Landau-Lifshitz-Gilbert (LLG) equation which describes the dynamics of a magnetic moment in the presence of a magnetic field. In a static magnetic field H_0, the magnetic moment will precess with the Larmor frequency ω_s. In detail, ω_s depends on the static field strength and on its orientation due to anisotropy [18]. This precessional motion can be resonantly excited by a time varying microwave magnetic field H_1 with a frequency close to ω_s. To observe spin pumping in FM/NM heterostructures, the field H_0 should be applied perpendicular to the interface normal (i.e., in the interface plane) [12,14,19,20]. In this case, the FMR dispersion (in the absence of crystalline magnetic anisotropy) is [21] $\omega_s = \gamma\mu_0\sqrt{H_0(H_0+M_s)}$. Here, M_s is the material specific saturation magnetization, γ is the material specific gyromagnetic ratio, and μ_0 is the vacuum permeability. In the limit $H_0 \gg M_s$ the resonance frequency is thus linear in magnetic field. Contrary to the magnon resonance frequency ω_s, the resonance frequency ω_c of a macroscopic cavity is determined by geometrical and dielectric parameters only and therefore usually does not depend on the magnetic field. However, since the magnonic mode (magnetization excitation) and the photonic mode (cavity excitation) interact in resonance, we expect modifications to the pure FMR and pure cavity dispersions. To be specific, we anticipate an anticrossing of the FMR and the cavity dispersion for a sufficiently strong magnon-photon coupling.

To describe the coupling between the cavity mode and the magnonic excitation, the quantum mechanical Tavis-Cummings model [22,23] and classical first principles [16] approaches using the input-output formalism [5] have successfully been used. For the dipolar interaction assumed in the models, the single spin-single photon coupling strength g_0 is proportional to the vacuum microwave magnetic field H_1^0 and the dipole moment m of the spin. In the scope of the Tavis-Cummings model, it has been shown that the collective coupling strength g_{eff} of an ensemble of many noninteracting spins to the vacuum microwave magnetic field of a cavity is proportional to the square root of the number N of polarized spins. In a classical theory, Cao *et al.* [16] derived that this $\sqrt{N}$ behavior prevails also for the magnon-photon coupling in magnetically ordered systems. Here, the total magnetization and thus the filling factor of the ferromagnetic material in the cavity can be used as a measure for the total number of spins.

The characteristic fingerprint of strong coupling is the formation of an observable anticrossing of the cavity and the magnon dispersion relation close to resonance. Note that the presence of strong coupling and a visible anticrossing of the dispersion relations requires that the effective coupling rate g_{eff} exceeds the loss rates of the spins (γ_s) and the cavity (κ_c). Experimentally, we tune the magnon resonance frequency ω_s across the cavity resonance frequency ω_c via an externally applied static magnetic field. The coupled system can most simply be modeled in the vicinity of the resonance frequency using two coupled harmonic oscillators, where the resonance frequency is [5]:

$$\omega_\pm = \omega_c + \frac{\Delta}{2} \pm \frac{1}{2}\sqrt{\Delta^2 + 4g_{\text{eff}}^2}. \tag{1}$$

Here, $\Delta = \gamma(\mu_0 H_0 - \mu_0 H_{\text{res}})$ is the spin-cavity detuning with H_{res} satisfying the magnon resonance condition for a given cavity frequency ω_c.

In ferromagnetic films, apart from the uniform FMR mode additional magnetic modes, so-called perpendicular standing spin waves modes appear due to magnetic boundary conditions. For the condition where the magnetization is pinned at least at one surface of the film (and in the absence of any anisotropies or magnetic gradients) the magnon spectrum can easily be calculated [21]. The difference of the resonance field of the nth mode from the fundamental ($n = 1$) mode $H_{\text{res}}^n - H_{\text{res}}^1$ is proportional to $(n-1)^2$. Cao *et al.* [16] also calculated the expected coupling strength for different modes and found that the coupling decreases with increasing mode number as $g_{\text{eff}} \propto 1/n$. This can be understood when considering the microwave mode profiles and the fact that the spatial mode profile of the microwave field H_1^0 in a cavity is typically homogeneous and in phase throughout the thickness of the (thin film) sample. Therefore only every second mode can be excited and the effective magnetization to which the microwave can couple to is reduced to $\frac{M_s}{n}$.

B. Spin pumping and strong coupling

Spin pumping in ferromagnet/normal metal bilayers in the weak coupling regime is well understood [12,14,20]: An additional mechanism which damps the magnetization precession becomes available by spin pumping, as the precessing magnetization is driving a spin current into the adjacent normal metal [14]. In electrically detected spin pumping, this spin current is then converted into a charge current via the inverse spin Hall effect (ISHE). For electrical open circuit conditions, one thus obtains a voltage which scales as [12,20] $V_{\text{SP}} \propto g^{\uparrow\downarrow}\lambda_{\text{SD}} \tanh\frac{t_N}{2\lambda_{\text{SD}}} \sin^2\theta$. It, thus, contains information on the spin mixing conductance $g^{\uparrow\downarrow}$, the spin diffusion length λ_{SD}, and the magnetization precession cone angle θ and depends on the thickness of the normal metal layer t_N. The maximal precession cone angle θ and thus the maximal expected spin pumping voltage depends on the microwave power but also on the coupling strength between cavity and spin system. For strong coupling, the cone angle is expected to be reduced as

compared to the weak coupling case due to the hybridized nature of the excitation at its maximal intensity.

The other contributions in the equation for V_{SP} are material constants: The spin mixing conductance $g^{\uparrow\downarrow}$ describes the transparency of the ferromagnet/normal metal interface and limits the spin pumping efficiency generally; the spin diffusion length λ_{SD} in conjunction with the normal metal thickness t_N accounts for a spin accumulation in the normal metal and reduces the spin pumping efficiency if $t_N \lessapprox \lambda_{SD}$. Furthermore, short circuiting of the generated spin pumping voltage via the normal metal layer reduces the detected voltage. For the YIG/Pt heterostructures this plays a role for Pt thicknesses considerably larger than the spin diffusion length $t_N \gg \lambda_{SD}$ [12].

III. EXPERIMENTAL DETAILS

A. Sample preparation

In our experiments we used YIG/Pt heterostructures grown by liquid phase epitaxy (LPE) on (111)-oriented gadolinum gallium garnet (GGG) substrates. The YIG film thickness was 2.8 μm. In order to produce a high quality interface between YIG and Pt, and thus a large spin mixing conductance $g^{\uparrow\downarrow}$, we followed the work of Jungfleisch *et al.* [24] and first treated the YIG surface by piranha etching for five minutes in ambient conditions. Thereafter, the sample was annealed at 500 °C for 40 minutes in an oxygen atmosphere of 25 µbar. Under high vacuum, it was then transferred into an electron beam evaporation chamber where 5 nm Pt was deposited. The exact Pt thickness was determined using x-Ray reflectometry. We note, however, that for our analysis the Pt layer thickness is of minor importance as it was larger than the spin diffusion length λ_{SD} of Pt such that the Pt layer simply serves as a perfect spin sink [25].

In order to achieve collective strong coupling between magnons and cavity photons, the number of magnetic moments must be sufficiently high. Therefore, we diced the sample into several pieces of different lateral dimensions. Magnetic resonance experiments in the strong coupling regime showed that the $\sqrt{N}$ scaling of the coupling strength discussed in Sec. II is indeed obeyed upon comparing samples with different volume and thus different total magnetic moment. In the following, we will focus on a sample with lateral dimensions 2 × 3 mm which, with the effective spin density $\rho_S = 2.1 \times 10^{22} \frac{\mu_B}{\text{cm}^3}$ of iron atoms in YIG [26], contains on the order of 4×10^{17} spins. Finally, the sample was mounted on a printed circuit board sample carrier and wire bonded as depicted in the inset of Fig. 1. The carrier itself was mounted on a sample rod which allowed the sample to be accurately positioned in the electrical field node of a Bruker Flexline MD5 dielectric ring cavity in an Oxford Instruments CF935 gas flow cryostat. Shielded DC cabling allowed for the measurement of the ISHE voltage. The detailed design blueprints of the sample rod and chip carrier can be retrieved online [27].

B. Experimental setup

The Bruker cavity exhibits a TE_{011} mode with an electric field node at the sample position. Its quality factor $Q = \omega/(2\kappa_c) = \omega/(2(\kappa_i + \kappa_e))$ is dominated by the dissipative losses in the dielectric and its finite electrical resistance (κ_i)

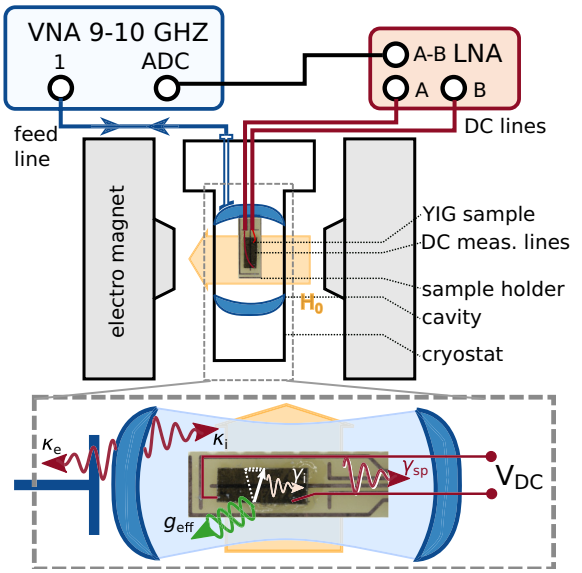

FIG. 1. Block diagram of the experimental setup including low noise voltage amplifer (LNA), vector network analyzer (VNA), and sample mounting. (Inset) Schematic of the coupling scheme illustrating cavity decay due to intrinsic losses (κ_i) and losses to the feed line (κ_e) and spin system decay consisting of intrinsic damping (γ_i) and spin pumping damping (γ_{sp}) as well the collective coupling rate g_{eff}.

as well as radiation back into the cavity feed line (κ_e). By changing the cavity's coupling ratio to the feed line, unloaded coupled quality factors Q_c from 0 to 8000 can be achieved. This allows tuning in and out of the strong coupling regime easily. Using the gas flow cryostat, different temperatures can be stabilized. All the following experiments have, however, been performed at room temperature.

To measure ferromagnetic resonance (FMR) the cavity was connected to the port of an Agilent N5242A vector network analyzer (VNA). The driving power of 15 dBm excites at maximum on the order of $N_{Ph} = P/(\hbar\omega\kappa_c) = 3 \times 10^{14}$ photons in the cavity which is considerably smaller than the number of spins in the sample (4×10^{17}). In this case, the theory presented in Sec. II is well justified [28]. The frequency dependent cavity reflection S_{11} was measured while sweeping the external field $\mu_0 H$ that is created by a water cooled electromagnet. The VNA's intermediate frequency (IF) bandwidth was chosen to be 100 Hz which leads to a frequency sweep time of approximately 2 s for each magnetic field step. A calibration of the microwave lines up to the resonator's SMA connector was performed. The calibration did not include the feed line inside the resonator mount, which gave rise to a background signal in the reflection parameter. However, by utilizing the full complex S parameter for the background subtraction with the inverse mapping technique outlined by Petersan and Anlage [29] and a subsequent Lorentzian fit to the magnitude, a reliable measurement of Q is still possible, even for a completely uncalibrated setup. We note that even though standing waves in the microwave feed line will not appear in the calibrated reflection measurement they will still change the total power in the cavity and therefore may complicate the electrically detected DC spin pumping signal. Uncalibrated measurements did not show sharp feed line resonances in

the frequency range studied here but only smooth oscillations with an amplitude change of less than 1 dB, and there was no correlation in the DC signal resolved. In order to fit the data and as it improves clarity, we only discuss calibrated measurements in the following.

The DC voltage from the sample was measured along the cavity axis and thus perpendicular to the external magnetic field and the sample normal. It was amplified with a low noise differential voltage amplifier (LNA) model 560 from Stanford Research Systems. The amplifier was operated in its low noise (4 nV/$\sqrt{\text{Hz}}$) mode and set to a gain of 2×10^4. The analog high-pass filter of the amplifier was disabled, however, a low-pass filter with a 6dB roll-off at 1 kHz was employed. Limiting the bandwidth of the amplifier by filtering is required in order to achieve a good signal-to-noise ratio. Care has, however, to be taken as the line shape may be quickly distorted by inappropriate settings and thus the signature of spin pumping might be masked. High-pass filtering can easily lead to a dispersivelike contribution to the signal, whereas low-pass filtering will give rise to asymmetric line shapes depending on the ratio of IF bandwidth and low-pass frequency. We made sure that no such distortions contribute to the presented measurements. The amplified voltage signal was finally recorded using the auxiliary input of the VNA simultaneously with the cavity reflection S_{11}.

IV. RESULTS AND DISCUSSION

We first focus on the case of the so-called critical coupling of the feed line to the cavity in which most FMR experiments are conducted. In this case, the internal loss rate of the cavity equals the loss rate to the feed line and the quality factor is $Q_c = \omega_r/2\kappa_i = Q_i/2$, i.e., half of the maximal quality factor Q_i of the cavity in the limit of negligible coupling to the feed line. Note that inserting a sample and holder into the cavity will reduce the cavity Q further by an amount which depends on the sample and holder details such as conductivity and dielectric losses. Based on our measured loaded $Q_c = 706$, the cavity decay rate is calculated to be $\kappa_c/2\pi = \frac{\omega_r}{2\pi}/2Q_c = 6.8$ MHz.

Strong coupling of the magnon and cavity system manifests itself in a characteristic anticrossing of the (magnetic field independent) cavity resonance frequency and the magnon dispersion that is (approximately) linear in magnetic field. This anticrossing corresponds to two distinct peaks in a line cut at the resonance field which are immediately visible in the reflection spectrum in Figs. 2(a)–2(c). The minimal splitting gives the collective coupling strength $g_{\text{eff}}/2\pi = 31.8$ MHz of the fundamental mode and any degenerate modes to the cavity. Taking into account the number of spins in the sample, the single spin coupling rate is on the order of $g_0/2\pi = 0.1$ Hz which is in agreement with experiments on paramagnetic systems [30].

In our setup, even the coupling of higher order spin wave modes to the cavity can be resolved. We number the spin waves as noted in Figs. 2 and 5 taking into account that with a uniform driving field only odd numbered modes can be excited [Fig. 3 (inset)]. In the anticrossing of the fundamental mode, at least one further spin wave mode can be observed and a slight asymmetry indicates that there are further modes that cannot be resolved. We start the numbering for the clearly

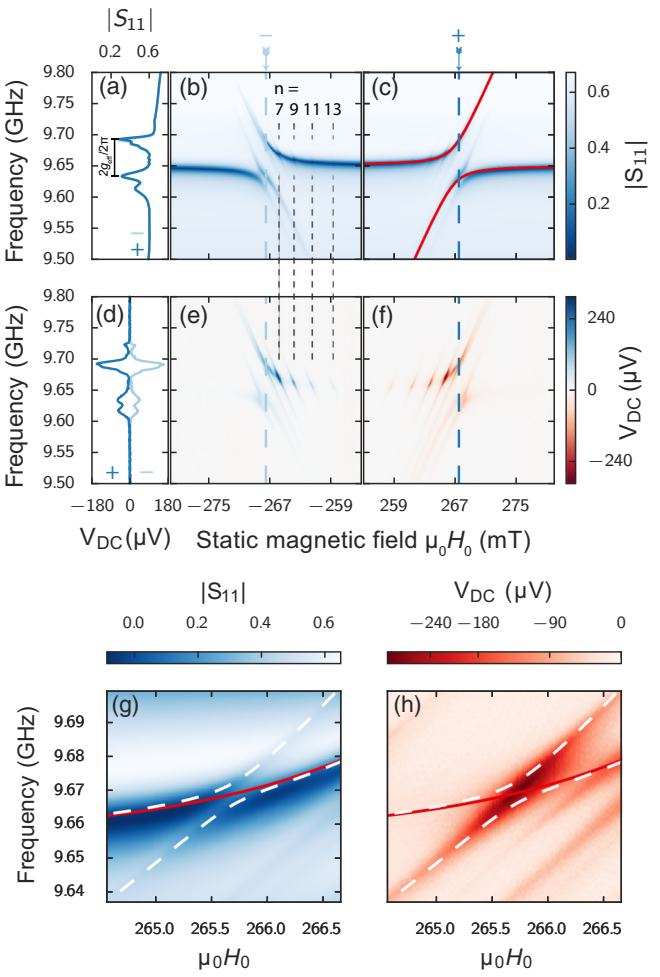

FIG. 2. (b),(c) Reflection parameter S_{11} recorded while sweeping the magnetic field and the microwave frequency. Strong coupling of the collective spin excitations is indicated by a clear anticrossing and spin wave modes to the low field side of the main resonance are visible. (e),(f) Simultaneously recorded DC voltage. Fundamental and spin wave modes are visible where the latter couple less strongly and thus pump spin current more efficiently. (a),(d) Line cuts at $H_0 = \pm 267.5$ mT show the symmetry under field reversal for S_{11} (a) and V_{DC} (d). (g),(h) Detail of the $n = 7$ spin wave mode in microwave reflection (g) and as voltage detected spectrum (h). Superimposed is the dispersion relation of the strong coupling between the fundamental FMR mode and the cavity as solid red line. The anticrossing of this hybrid and the $n = 7$ spin wave mode is displayed as dashed white lines.

separated spin waves as depicted in Fig. 2(a) with $n = 7$. The resonance fields of the spin wave modes (inset of Fig. 5) agree well with the anticipated $H^n_{\text{res}} - H^1_{\text{res}} \propto n^2$ behavior for this numbering. Furthermore, the resonance fields can be quantitatively modeled accurately with values of the exchange stiffness, M_s and γ reported in literature [31–33].

The resonance field of the lowest order spin wave mode $n = 5$ is very close to the resonance field of the fundamental resonance and is thus difficult to analyze quantitatively. The $n = 7$ spin wave mode exhibits the largest effective coupling (3 MHz) of the other spin wave modes. It is shown in Figs. 2(g) and 2(h) in detail. The red and white lines correspond to the harmonic-oscillator model [Eq. (1)] for the fundamental mode

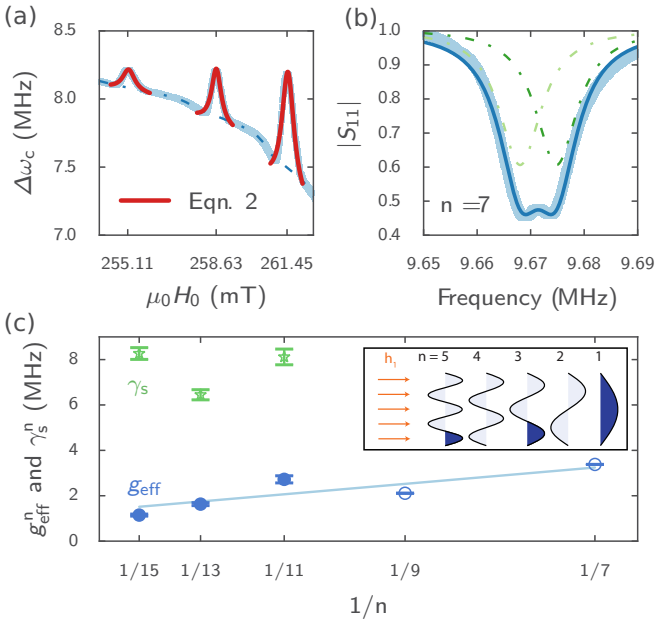

FIG. 3. (a) Half width at half maximum linewidths (light blue) from fits of a Lorentzian to frequency cuts at fixed fields. Fitting Eq. (2) for each spin wave resonance enables extraction of the coupling strength for weakly coupled spin waves [34]. (b) For the more strongly coupling spin wave modes ($n = 7,9$), the model of Eq. (2) overestimates the coupling strength. Instead, the sum of two Lorentzian absorption peaks (dashed, sum as solid dark blue line) are fitted to a cut at constant field $\mu_0 H_0 = 266.17$ mT (light blue); the splitting of the centers is equal to $2g_{\rm eff}/2\pi$. (c) Spin wave-cavity coupling strength $g^n_{\rm eff}$ and spin decay rate γ^n_s as a function of the inverse mode number. Also displayed is the predicted $1/n$ behavior. Inset: A homogeneous excitation microwave field h_1 couples only to the part of the dynamic magnetization of a spin wave mode that has no corresponding π-phase shifted component. For the shown pinned boundary conditions only odd modes can be excited, where the effective magnetization (blue) scales as $1/n$.

and $n = 7$ spin wave mode, respectively. As the spin wave couples to an already hybridized system, we superimposed the dispersion $\omega_c = \omega_r(B)$ of the hybridized system of fundamental mode and unperturbed cavity as the "cavity" mode in the modeling of the spin wave mode couplings.

In order to quantify the coupling strength of the higher order modes which only interact weakly with the hybridized cavity-fundamental FMR mode ($n = 11,13,15$), we follow the approach of Herskind *et al.* [34]. For each field, we fit a Lorentzian to the magnitude of the cavity absorption. From this fit, we can extract the resonance frequency ω_c and the half width at half maximum (HWHM) linewidth $\Delta\omega$ of the absorption signal [Fig. 3(a)]. We start with removing the slope in the data which originates from the strong coupling between the fundamental FMR mode and the cavity mode. The evolution of the HWHM linewidth for the coupling with each weakly coupled spin wave mode can then be separately modeled as [34]

$$\Delta\omega = \Delta\omega_c + g^2_{\rm eff}\gamma_s/\left(\gamma_s^2 + \Delta^2\right). \quad (2)$$

This relation allows us to extract the spin wave-cavity coupling strength $g^n_{\rm eff}$ for each weakly coupled spin wave mode. The coupling strength of the spin waves to the already hybridized cavity resonance decreases with the order of the mode. This can be understood by taking into account that the effective magnetic moment to which the homogeneous microwave field can couple decreases with increasing mode number. For the more strongly coupled spin wave modes ($n = 7$ and 9), we determine the effective coupling strength from the splitting of two fitted Lorentzian absorption peaks. This is exemplarily shown in Fig. 3(b). The extracted values, shown in Fig. 3(c), match with the also shown theoretically expected $\frac{1}{n}$ dependence of the coupling strength [16]. We note, however, that the range of $1/n$ values is limited and we therefore consider that $g^\infty_{\rm eff} = 0$ to obtain a reliable fit. From this fit we can extrapolate an effective coupling of the $n = 1$ mode, the fundamental mode, of 22.7 ± 1.9 MHz. This value deviates from the effective coupling extracted from the main anticrossing [Fig. 2(a)] by 9.1 MHz. The discrepancy can be resolved by taking into account that the magnon mode $n = 3$ is not resolved. Thus, the previously measured coupling rate of 31.8 MHz is comprised of the $n = 3$ and the $n = 1$ mode. With an extrapolated value of 7.6 MHz for the coupling rate of the $n = 3$ mode, the coupling rate of the fundamental mode exclusively calculates to $g^1_{\rm eff}/2\pi = 24.2$ MHz which is in agreement with the extrapolated value.

The ratio of the effective coupling rate and the spin decay rate γ_s [Fig. 3(c)] confirms that the higher order spin waves couple weakly to the cavity whereas the $n = 7$ and $n = 9$ spin wave modes are already in an intermediate coupling regime and need to be analyzed separately.

Additionally, in Fig. 2 we observe a secondary anticrossing at a field higher than the fundamental mode which stems from an unidentified mode. A similar feature was found in other experiments [15] and has been interpreted in the same manner. In our data, we can clearly distinguish between the fundamental mode and this additional mode—simply by remembering that the relative intensity and coupling strength is expected to be higher for the fundamental mode. Possible origins for this additional mode are an inhomogeneous sample or a gradient in the magnetic properties across the film thickness [35]. Lastly, we note that the recorded signal in the reflection parameter is completely symmetric upon magnetic field reversal.

Next, we turn to the voltage detected response of the system shown in Figs. 2(d)–2(f). Contrary to the reflection parameter, the voltage signal reverses sign on inverting $\mu_0 H_0$ Fig. 2(d). The line shape that we record for all individual modes is completely symmetric as far as they can be clearly distinguished from each other. This is the anticipated signature of a voltage caused by spin pumping only in FMI/NM bilayer [13]. We thus conclude that we observe a signal purely caused by spin pumping and not by any rectification effect. In a FMI/NM bilayer ($\rho_{\rm YIG} \geqslant 10$ GΩm) [36] rectification can only arise from a change of the spin Hall magnetoresistance (SMR) in the normal metal in combination with a high frequency current in the Pt. According to model calculations [13] this effect is negligible for the system we investigate because of the small magnitude of the SMR effect (<0.1%). This notion is further corroborated by the fact that the change in line shape expected for rectification type signals is not visible in our data. Apart from the spin wave modes which

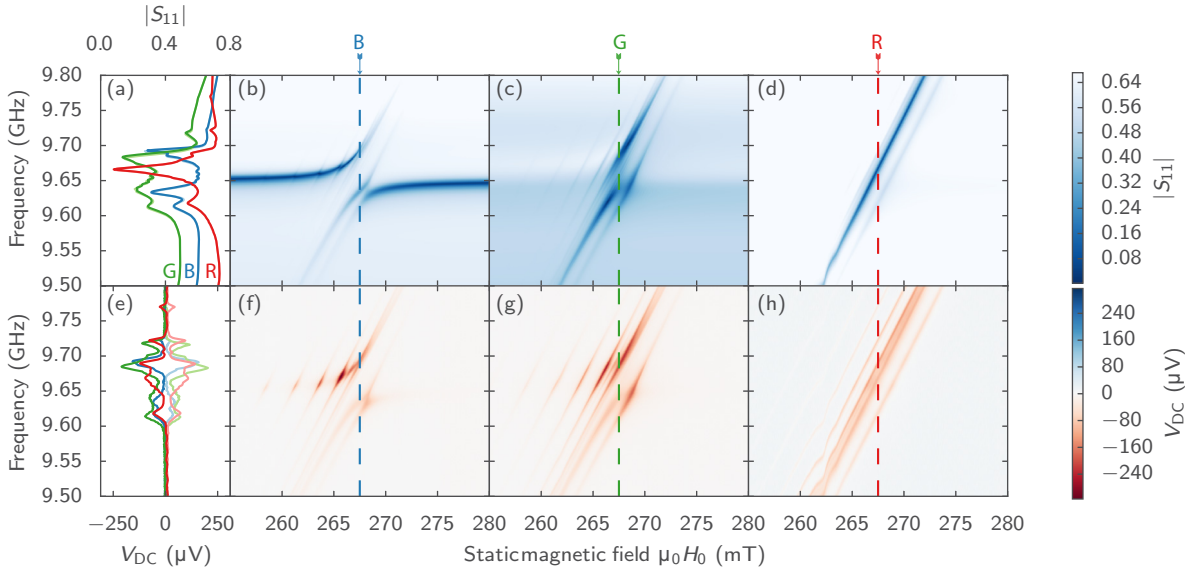

FIG. 4. Increasing the coupling of the cavity to the feed line (from left to right) increases the cavity loss rate κ_c and thus linewidth $\Delta\omega/2\pi$. This enables experimental control of the transition between strong and weak coupling. (b)–(d) Microwave reflection. (f)–(h) DC voltage. (a),(e) Line cuts at fixed field ($H_0 = \pm 267.5$ mT) are shown for the different coupling regimes (R, G, B and corresponding colors) in both reflection (a) and voltage (e) measurements. They clearly show the merging of the two dispersion curves during the strong/weak transition. Cuts at positive field (intense colors) and negative field (pale colors) again confirm the symmetry, $V(-H_0) = -V(H_0)$ and $S_{11}(-H_0) = S_{11}(H_0)$.

are well resolved in the DC voltage signal, we can also clearly see the electrically detected spin pumping voltage originating from the hybridized system of cavity and fundamental FMR mode (the main anticrossing). This strongly hybridized mode can, however, pump spin current into the normal metal only very inefficiently and thus the DC voltage we observe is small. In the voltage detected response, we can distinguish the spin wave modes and their coupling to the cavity mode too [Figs. 2(d)–2(f)]. Figure 2(h) shows the $n = 7$ spin wave mode with the same model of two coupled harmonic oscillators as in Fig. 2(g). The resonance position and dispersion of the spin wave reproduces the behavior detected via the microwave reflection. The anticrossing that is visible in the microwave reflection cannot be clearly observed in the voltage detected response for this weakly coupled mode. This is due to the fact that the voltage signal is strongest when the hybridization is largest. For a weakly coupled mode, due to the large linewidth, the signal from the upper and the lower branch of the anticrossing overlap giving rise to the observed shape.

The upper panels (b)–(d) of Fig. 4 show the change in cavity reflection as we gradually increase the coupling of the cavity to the feed line and thus increase the cavity decay rate. Starting from the critically coupled case (internal cavity losses are equal to losses into the feed line) in panel (b) to a highly overcoupled cavity (losses into the cavity feed line dominate the cavity's decay rate) in panel (d), we clearly see an increase in the cavity linewidth up to the point were the unperturbed cavity is no longer recognizable.

This changes the appearance of the magnetic resonance drastically: In the critically coupled case the cavity also acts as a filter for the probing microwaves. Thus, the resonances cannot be observed at frequencies far from the unperturbed cavity resonance frequency. Therefore, no resonant absorption is observed at 9.80 and 9.50 GHz in Fig. 4(b). As the quality of the cavity and thus the quality of the filter is reduced, the resonances can be observed over a broader frequency range. In the intermediate case shown in panel (c), effects of the magnon-cavity coupling can still be observed. The fundamental mode's dispersion is distorted near the cavity resonance frequency. In the extremely overcoupled case, the microwave reflection $|S_{11}|$ is essentially flat over the observed frequency range at frequencies where no FMR is expected [panel (d)]. The response of the system then shows the dispersion of the magnon system directly. Multiple diagonal lines of high absorption corresponding to the dispersion of the individual spin wave modes can be observed. From their slope, the true g factor and the effective magnetization M_{eff} can be estimated. For the well separated $n = 9$ spin wave mode, we extract $g = 2.0$ and $M_{\text{eff}} = 147$ kA m^{-1} which are both in good agreement with corresponding values for YIG reported in literature [31,32].

In the same way as the cavity linewidth, the cavity decay rate increases from left to right and, in turn, the microwave magnetic field strength H_1 in the cavity decreases. For the already weakly coupled spin wave modes the spin pumping voltage decreases with decreasing microwave magnetic field strength H_1 (indicated by the higher S_{11} parameter) in the cavity. The DC spin pumping voltage amplitude corresponding to the fundamental mode [Figs. 4(f)–4(h)] does, however, not decrease for lower Q factors but stays approximately constant. This behavior can be understood considering that the absorbed power of the cavity-spin system stays approximately constant when changing the cavity decay rate [Fig. 4(a)] and the fact that the absolute effective coupling strength g_{eff} does not change when changing the cavity decay rate.

The best measure of the true magnon spectrum and linewidths of the spin system can be extracted from the highly overcoupled case [Figs. 4(d) and 4(h) and Fig. 5]. There, the magnon-photon coupling is negligible compared to the cavity loss rate and therefore, the magnon-cavity mode

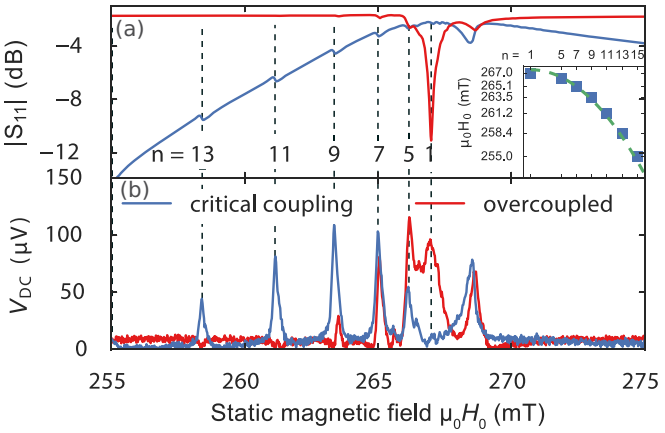

FIG. 5. Line cuts of (a) reflection parameter and (b) DC voltage at the resonator frequency $\omega_c(H_0 = 0) = 9.651$ GHz. In the strongly coupled magnon-photon case (blue lines, cavity and feed line are critically coupled) the only indication of the fundamental mode ($n = 1$) is the large slope in $|S_{11}|$ whereas in the weakly coupled case (red lines, cavity and feed line are highly overcoupled) the magnon spectrum is accurately and clearly reproduced. Inset: Spin wave resonance fields extracted from the weakly coupled case (blue squares) and resonance fields anticipated with values from literature [31–33] (green dashed line).

hybridization does not distort the dispersion. A mode that strongly couples with the cavity, on the contrary, can vanish completely in the fixed-frequency spectrum. This is shown exemplarily in Fig. 5(a): In the weakly coupled case (cavity and feedline are highly overcoupled), the fundamental mode is easily distinguishable by its amplitude. In the strongly coupled case (critical cavity feedline coupling), however, the fundamental mode can only be observed as a broad slope in the data and linewidth or resonance position cannot be extracted. The same situation is observed in the spin pumping voltage [Fig. 5(b)]. There, the intensity connected with the fundamental mode is reduced even further by the low spin pumping efficiency of a strongly hybridized mode. In the weakly coupled case, on the other hand, the fundamental mode appears as a distinct peak. We finally note that we observe the described anticrossing due to the magnon-photon coupling and thus the distortion of the lines in a fixed-frequency experiment (with the cavity tuned to high Q, as usually done in cavity-based FMR experiments) already for sample volumes as small as $V = 2 \times 10^{-3}$ mm^3 in the case of YIG ($M_S = 140$ kA m^{-1}) [32]. These sample volumes are easily achieved for LPE grown samples, suggesting that in most cavity FMR experiments [37] the effects of the coupling need to be taken into account in order to yield accurate results (especially in magnetic resonance systems with automatic frequency control).

V. CONCLUSIONS

In summary, we presented systematic measurements of spin pumping in different regimes of the magnon-photon coupling strength. For the fundamental mode of a YIG/Pt bilayer, strong coupling with an effective coupling strength of $g^1_{\mathrm{eff}}/2\pi = 22.7$ MHz has been achieved at room temperature in a standard EPR cavity. The characteristics of the coupled magnon-photon system fit well to the established theory and are consistent with recent results. Simultaneously, we recorded the electrically detected spin pumping signal of the fundamental mode. We were able to tune the system from the strong to the weak coupling regime by changing the cavity's decay rate. The evolution of the spin pumping signal of the fundamental mode has been analyzed qualitatively and follows the predictions of Lotze [17]: In the strongly coupled magnon-photon system the spin pumping efficiency is reduced as the precession cone angle is smaller than in the weakly coupled case. Additionally, we were able to observe coupling and electrically detected spin pumping of several spin wave modes with distinctly different coupling strengths which exhibit the $1/n$ dependence predicted by Cao *et al.* [16]. We used this behavior to disentangle contributions of higher order spin waves and the fundamental mode to the observed main anticrossing. Furthermore, we directly demonstrated the implications of strong coupling on fixed-frequency FMR experiments. We conclude that small sample volumes or a highly overcoupled cavity are mandatory for a qualitatively and quantitatively correct evaluation of the magnon spectrum and damping.

ACKNOWLEDGMENTS

We thank Christoph Zollitsch and Johannes Lotze for many valuable discussions and Michaela Lammel for assistance in the sample preparation. M. Harder acknowledges support from the NSERC MSFSS program. We gratefully acknowledge funding via the priority program Spin Caloric Transport (spinCAT) of Deutsche Forschungsgemeinschaft (Project GO 944/4), collaborative reserach center (SFB) 631, project C3 and the priority program SPP 1601 (HU 1896/2-1).

[1] D. I. Schuster, A. P. Sears, E. Ginossar, L. DiCarlo, L. Frunzio, J. J. L. Morton, H. Wu, G. A. D. Briggs, B. B. Buckley, D. D. Awschalom, and R. J. Schoelkopf, Phys. Rev. Lett. **105**, 140501 (2010).

[2] Y. Kubo, F. R. Ong, P. Bertet, D. Vion, V. Jacques, D. Zheng, A. Dréau, J.-F. Roch, A. Auffeves, F. Jelezko, J. Wrachtrup, M. F. Barthe, P. Bergonzo, and D. Esteve, Phys. Rev. Lett. **105**, 140502 (2010).

[3] C. W. Zollitsch, K. Mueller, D. P. Franke, S. T. B. Goennenwein, M. S. Brandt, R. Gross, and H. Huebl, Appl. Phys. Lett. **107**, 142105 (2015).

[4] O. O. Soykal and M. E. Flatté, Phys. Rev. Lett. **104**, 077202 (2010).

[5] H. Huebl, C. W. Zollitsch, J. Lotze, F. Hocke, M. Greifenstein, A. Marx, R. Gross, and S. T. B. Goennenwein, Phys. Rev. Lett. **111**, 127003 (2013).

[6] Y. Tabuchi, S. Ishino, T. Ishikawa, R. Yamazaki, K. Usami, and Y. Nakamura, Phys. Rev. Lett. **113**, 083603 (2014).

[7] N. Kostylev, M. Goryachev, and M. E. Tobar, Appl. Phys. Lett. **108**, 062402 (2016).

[8] X. Zhang, C.-l. Zou, L. Jiang, and H. X. Tang, Phys. Rev. Lett. **113**, 156401 (2014).

[9] X. Zhang, C.-l. Zou, N. Zhu, F. Marquardt, L. Jiang, and H. X. Tang, Nat. Commun. **6**, 8914 (2015).
[10] N. J. Lambert, J. A. Haigh, S. Langenfeld, A. C. Doherty, and A. J. Ferguson, Phys. Rev. A **93**, 021803 (2016).
[11] B. M. Yao, Y. S. Gui, Y. Xiao, H. Guo, X. S. Chen, W. Lu, C. L. Chien, and C.-M. Hu, Phys. Rev. B **92**, 184407 (2015).
[12] F. D. Czeschka, L. Dreher, M. S. Brandt, M. Weiler, M. Althammer, I.-M. Imort, G. Reiss, A. Thomas, W. Schoch, W. Limmer, H. Huebl, R. Gross, and S. T. B. Goennenwein, Phys. Rev. Lett. **107**, 046601 (2011).
[13] R. Iguchi, K. Sato, D. Hirobe, S. Daimon, and E. Saitoh, Appl. Phys. Exp. **7**, 013003 (2014).
[14] Y. Tserkovnyak, A. Brataas, and G. E. W. Bauer, Phys. Rev. Lett. **88**, 117601 (2002).
[15] L. Bai, M. Harder, Y. P. Chen, X. Fan, J. Q. Xiao, and C.-M. Hu, Phys. Rev. Lett. **114**, 227201 (2015).
[16] Y. Cao, P. Yan, H. Huebl, S. T. B. Goennenwein, and G. E. W. Bauer, Phys. Rev. B **91**, 094423 (2015).
[17] J. Lotze, Ph.D. thesis, Technische Universität München, 2015.
[18] A. Brandlmaier, S. Geprägs, M. Weiler, A. Boger, M. Opel, H. Huebl, C. Bihler, M. S. Brandt, B. Botters, D. Grundler, R. Gross, and S. T. B. Goennenwein, Phys. Rev. B **77**, 104445 (2008).
[19] B. Heinrich, Y. Tserkovnyak, G. Woltersdorf, A. Brataas, R. Urban, and G. E. W. Bauer, Phys. Rev. Lett. **90**, 187601 (2003).
[20] O. Mosendz, J. E. Pearson, F. Y. Fradin, G. E. W. Bauer, S. D. Bader, and A. Hoffmann, Phys. Rev. Lett. **104**, 046601 (2010).
[21] C. Kittel, *Introduction to Solid State Physics* (John Wiley and Sons, New York, 1995).
[22] M. Tavis and F. W. Cummings, Phys. Rev. **170**, 379 (1968).
[23] J. M. Fink, R. Bianchetti, M. Baur, M. Göppl, L. Steffen, S. Filipp, P. J. Leek, A. Blais, and A. Wallraff, Phys. Rev. Lett. **103**, 083601 (2009).
[24] M. B. Jungfleisch, V. Lauer, R. Neb, a. V. Chumak, and B. Hillebrands, Appl. Phys. Lett. **103**, 022411 (2013).
[25] M. Althammer, S. Meyer, H. Nakayama, M. Schreier, S. Altmannshofer, M. Weiler, H. Huebl, S. Geprägs, M. Opel, R. Gross, D. Meier, C. Klewe, T. Kuschel, J.-M. Schmalhorst, G. Reiss, L. Shen, A. Gupta, Y.-T. Chen, G. E. W. Bauer, E. Saitoh, and S. T. B. Goennenwein, Phys. Rev. B **87**, 224401 (2013).
[26] M. A. Gilleo and S. Geller, Phys. Rev. **110**, 73 (1958).
[27] The designs of the sample holder are published under the CERN Open Hardware License, http://hannes.maier-flaig.de/flexline-sample-rod.
[28] I. Chiorescu, N. Groll, S. Bertaina, T. Mori, and S. Miyashita, Phys. Rev. B **82**, 024413 (2010).
[29] P. J. Petersan and S. M. Anlage, J. Appl. Phys. **84**, 3392 (1998).
[30] E. Abe, H. Wu, A. Ardavan, and J. J. L. Morton, Appl. Phys. Lett. **98**, 251108 (2011).
[31] J. F. Dillon, Phys. Rev. **105**, 759 (1957).
[32] P. Hansen, P. Röschmann, and W. Tolksdorf, J. Appl. Phys. **45**, 2728 (1974).
[33] S. Klingler, A. V. Chumak, T. Mewes, B. Khodadadi, C. Mewes, C. Dubs, O. Surzhenko, B. Hillebrands, and A. Conca, J. Phys. D **48**, 015001 (2015).
[34] P. F. Herskind, A. Dantan, J. P. Marler, M. Albert, and M. Drewsen, Nat. Phys. **5**, 494 (2009).
[35] B. Hoekstra, R. P. van Stapele, and J. M. Robertson, J. Appl. Phys. **48**, 382 (1977).
[36] A. Tucciarone and P. De Gasperis, Thin Solid Films **114**, 109 (1984).
[37] Y. Kajiwara, K. Harii, S. Takahashi, J. Ohe, K. Uchida, M. Mizuguchi, H. Umezawa, H. Kawai, K. Ando, K. Takanashi, S. Maekawa, and E. Saitoh, Nature (London) **464**, 262 (2010).